

Zinc-Doping Strategy on P2-Type Mn-Based Layered Oxide Cathode for High-Performance Potassium-ion Batteries

Yunshan Zheng, Junfeng Li, Shunping Ji, Kwan San Hui,* Shuo Wang, Huifang Xu, Kaixi Wang, Duc Anh Dinh, Chenyang Zha, Zongping Shao,* and Kwun Nam Hui*

Mn-based layered oxide is extensively investigated as a promising cathode material for potassium-ion batteries due to its high theoretical capacity and natural abundance of manganese. However, the Jahn–Teller distortion caused by high-spin Mn^{3+} ($t_{2g}^3 e_g^1$) destabilizes the host structure and reduces the cycling stability. Here, $\text{K}_{0.02}\text{Na}_{0.55}\text{Mn}_{0.70}\text{Ni}_{0.25}\text{Zn}_{0.05}\text{O}_2$ (denoted as KNMNO-Z) is reported to inhibit the Jahn–Teller effect and reduce the irreversible phase transition. Through the implementation of a Zn-doping strategy, higher Mn valence is achieved in the KNMNO-Z electrode, resulting in a reduction of Mn^{3+} amount and subsequently leading to an improvement in cyclic stability. Specifically, after 1000 cycles, a high retention rate of 97% is observed. Density functional theory calculations reveals that low-valence Zn^{2+} ions substituting the transition metal position of Mn regulated the electronic structure around the Mn–O bonding, thereby alleviating the anisotropic coupling between oxidized O^{2-} and Mn^{4+} and improving the structural stability. $\text{K}_{0.02}\text{Na}_{0.55}\text{Mn}_{0.70}\text{Ni}_{0.25}\text{Zn}_{0.05}\text{O}_2$ provided an initial discharge capacity of 57 mAh g^{-1} at 100 mA g^{-1} and a decay rate of only 0.003% per cycle, indicating that the Zn-doped strategy is effective for developing high-performance Mn-based layered oxide cathode materials in PIBs.

Among the various application technologies, lithium-ion batteries (LIBs) are considered to be the most popular technology due to their high voltage ($>3.6 \text{ V}$) and energy density (120 Wh kg^{-1}) and long cycle life.^[3] However, the expansion in energy storage applications inevitably increases the manufacturing cost of LIBs due to the limited and uneven distribution of lithium resources in the Earth's crust.^[4,5] Compared with LIBs, sodium-ion batteries (SIBs) and potassium-ion batteries (PIBs) become two promising alternatives because of their more abundant resources and the same intercalation chemistry as LIBs.^[6–8] In particular, the lower standard redox potential of K/K^+ (-2.936 V vs SHE) makes PIBs a superior alternative to SIBs by converting to a higher operating voltage and energy density.^[9]

Layered transition metal oxides possessing high theoretical energy density and high K diffusion rates are widely used as cathode materials for PIBs.^[10–12] Typical Mn-based layered oxide materials

$[\text{K}_x\text{Mn}_{1-y}\text{M}_y\text{O}_2$ ($\text{M} = \text{Mn}, \text{Ni}, \text{Fe}, \text{etc.}$)] have attracted much attention due to their unique structural advantages and natural abundance of Mn.^[13,14] Among these layered oxides, P2-type $\text{K}_x\text{Mn}_{1-y}\text{M}_y\text{O}_2$ generally has a lower K^+ diffusion barrier and higher ionic conductivity, leading to better electrochemical performance and great potential for practical applications.^[15–19] However, Mn-based layered oxides contain the mixed valence of

1. Introduction


Energy storage technologies have received significant attention in smoothing and ensuring the supply of electricity from intermittent renewable energy sources, such as wind and solar.^[1–3]

Y. Zheng, J. Li, S. Ji, S. Wang, H. Xu, K. Wang, C. Zha, K. N. Hui
Joint Key Laboratory of the Ministry of Education
Institute of Applied Physics and Materials Engineering
University of Macau
Avenida da Universidade
Taipa, Macau SAR 999078, China
E-mail: bizhui@um.edu.mo

K. S. Hui
School of Engineering
Faculty of Science
University of East Anglia
NR4 7TJ Norwich, UK
E-mail: k.hui@uea.ac.uk

D. A. Dinh
VKTech Research Center
NTT Hi-Tech Institute
Nguyen Tat Thanh University
700000 Ho Chi Minh City, Vietnam

Z. Shao
State Key Laboratory of Materials-Oriented Chemical Engineering
College of Chemical Engineering
Nanjing Tech University
211816 Nanjing, China
E-mail: shaozp@njtech.edu.cn

 The ORCID identification number(s) for the author(s) of this article can be found under <https://doi.org/10.1002/smll.202302160>

© 2023 The Authors. Small published by Wiley-VCH GmbH. This is an open access article under the terms of the Creative Commons Attribution License, which permits use, distribution and reproduction in any medium, provided the original work is properly cited.

DOI: 10.1002/smll.202302160

Mn³⁺ and Mn⁴⁺. Mn⁴⁺ can form undistorted (ideal) [MnO₆] octahedra, which form stable crystal structures. However, high-spin Mn³⁺ with a (t_{2g})³(e_g)¹ electronic configuration in the 3D orbital usually causes Jahn–Teller distortions.^[20–22] In addition, the Mn valence fluctuates between +3 and +4 during the charging and discharging processes; as such, Jahn–Teller distortions will be repeatedly removed and restored, leading to irreversible multiphase transition.^[23] Therefore, inhibiting the severe Jahn–Teller distortion of massive Mn³⁺ and improving the structural stability of Mn-based layered oxides for durable cycling stability are important.

The strategy of the substitution of low-valence cations, such as Zn, Co, Mg, and Ni, of the P2 Mn-based layered oxide cathode has been successfully utilized to decrease the Mn³⁺ ratio to suppress the Jahn–Teller distortion and improve the structural and cycling stability in LIBs and NIBs.^[20,21,24,25] Xiao et al.^[20] reported the regulation of the Mn average valence by the substitution of Mn with Ti⁴⁺ and Mg²⁺ ions, which are effective to increase the Mn average valence in K_{0.5}Mn_{0.6}Co_{0.2}Fe_{0.1}Mg_{0.1}O₂ cathode in PIBs, leading to outstanding cycling stability with capacity retention of 91% after 150 cycles at 0.1 A g⁻¹. Bai et al.^[26] and Zhang et al.^[27] efficiently suppressed the Jahn–Teller distortion by increasing Mn average valence in K_{0.67}Mn_{0.83}Ni_{0.17}O₂ and K_{0.3}Mn_{0.95}Co_{0.05}O₂ cathodes through nickel and cobalt doping, respectively, leading to superior rate performance and cycling. K_{0.67}Mn_{0.83}Ni_{0.17}O₂ shows discharge capacities of 120, 91, 85, 77, and 65 mAh g⁻¹ at current rates of 0.2, 0.5, 1, 2, and 5 C, respectively. At a current density of 173 mA g⁻¹, the capacity retention in K_{0.3}Mn_{0.95}Co_{0.05}O₂ is about 75% of the initial capacity after 500 cycles. However, further studies aimed to develop a new strategy and understand the changes in the K_xMn_{1-y}M_yO₂ structure during charge–discharge cycling to improve the electrochemical performance in the application of PIBs

Considering that the Jahn–Teller distortion is mainly caused by Mn³⁺ ions, this study conducted divalent Zn-doping strategy in P2-type K_{0.02}Na_{0.55}Mn_{0.70}Ni_{0.25}Zn_{0.05}O₂ (denoted as KNMNO-Z) to stabilize its structure during the electrochemical process. Na-containing P2-type Mn-based layered oxide was chosen as the cathode because the introduction of Na can activate the redox reaction of transition metal ions and result in enhanced capacity.^[28] The KNMNO-Z electrode delivered an initial discharge capacity of 57 mAh g⁻¹ with a retention rate of 97% at 100 mA g⁻¹ and a decay rate of only 0.003% per cycle after 1000 cycles. The remarkable performance was mainly attributed to the fact that the Zn-doping strategy not only alleviates the Jahn–Teller distortion by increasing the average oxidation state of Mn but also reduces the inherent phase instability. Meanwhile, the structure evolution of the electrode has been investigated by several analytical techniques. According to density functional theory (DFT) calculations, Zn substitution can regulate the electronic structure around the Mn–O bond, thereby alleviating the anisotropic coupling between oxidized O²⁻ and Mn⁴⁺ and maintaining structural stability. This work may provide a rational strategy to improve the phase stability and electrochemical properties of Mn-based layered oxide cathode materials for PIBs.

2. Results and Discussion

The schematic illustration of the preparation process of KNMNO-Z is shown in **Figure 1**, which consists of two main steps. First, the Mn_{0.75}Ni_{0.25}CO₃ precursors were synthesized through the solvothermal method at 180 °C for 24 h.^[29] The collected Mn_{0.75}Ni_{0.25}CO₃ precursors were homogeneously mixed with K₂CO₃, ZnO, NaCl, and KCl and then calcined in air at 800 °C for 12 h. After cooling down to room temperature, KNMNO-Z was obtained by washing, filtering, and drying with water and ethanol. The control samples of K_{0.02}Na_{0.72}Mn_{0.75}Ni_{0.25}O₂ (denoted as KNMNO) and K_{0.26}Mn_{0.75}Ni_{0.25}O₂ (denoted as KMNO) were also prepared by a similar method as KNMNO-Z. **Figure 1** presents a schematic representation of the KNMNO-Z structure both before and after cycling. Notably, the structure of the KNMNO-Z electrode was found to remain stable throughout the cycling process, as demonstrated by the diagram.

The morphology and structure of the samples can be characterized by scanning electron microscopy (SEM) and transmission electron microscopy (TEM). As shown in **Figure S1**, Supporting Information, the structure of the Mn_{0.75}Ni_{0.25}CO₃ precursor consisted of uniform assembled microsphere structure with a diameter of ≈4–5 μm, as confirmed through X-ray diffraction (XRD) (**Figure S4**). The Mn_{0.75}Ni_{0.25}CO₃ precursor was assembled by submicron-cubic primary particles. KMNO (**Figure S2**, Supporting Information) is relatively spherical in shape and has an average diameter of 1–2 μm. With the doping of Na, a similar spherical shape was obtained (**Figure S3**, Supporting Information). The EDS mapping image confirmed the existence and uniform distribution of K, Na, Mn, and Ni in KNMNO and K, Mn, and Ni in the KMNO samples (**Figures S2c** and **S3c**, Supporting Information). The particles of KNMNO-Z are looser than those of KMNO and KNMNO (**Figure 2a**), which is conducive to providing sufficient contact between the electrode and the electrolyte to accelerate the electrochemical reaction kinetics. The TEM image (**Figure 2b**) and high-resolution TEM (HRTEM) image (**Figure 2c**), demonstrate the clear lattice fringes with interplanar spacings of 0.225 and 0.254 nm corresponding to the (102) and (100) planes with the typical P2-type layered structure, as verified by the selected area electron diffraction (SAED) pattern (**Figure 2d**). Finally, K, Na, Mn, Ni, Zn, and O are evenly distributed in the KNMNO-Z grain in the EDS mapping image (**Figure 2e** and **Table S1**).

The XRD patterns of the prepared KNMO material (**Figure S5**, Supporting Information) can be indexed well based on the phase K₂Mn₄O₈ (PDF Card No. 16–0205). Besides the main phase, the presence of NiO impurity can be detected.^[2] The crystal structure of KNMNO-Z material was studied by powder XRD analysis. **Figure 2f** shows the Rietveld refinement of KNMNO-Z, indicating a P2 material with the P63/mmc space group. No other phases were found, confirming the phase purity of the prepared samples. The calculated lattice parameters a = 2.88485 Å and c = 11.15580 Å are consistent with those of other typical P2-type layered K intercalation compounds. Results showed that KNMNO-Z possessed a typical hexagonal compact packing (hcp) crystal with layered ABBA stacking.^[19,30] In **Figure S6**, Supporting Information, the Rietveld refinement of KNMNO also shows a hexagonal

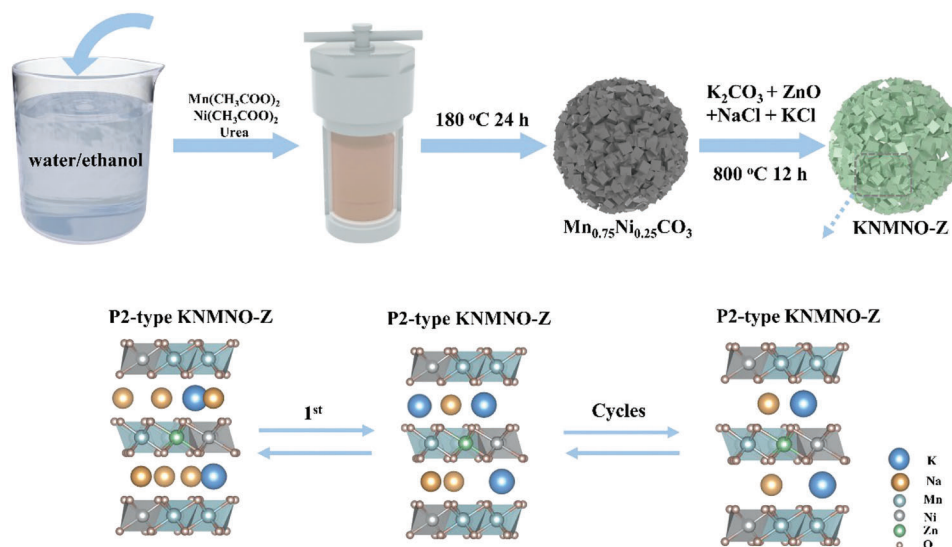


Figure 1. A schematic diagram of the fabrication process of KNMNO-Z.

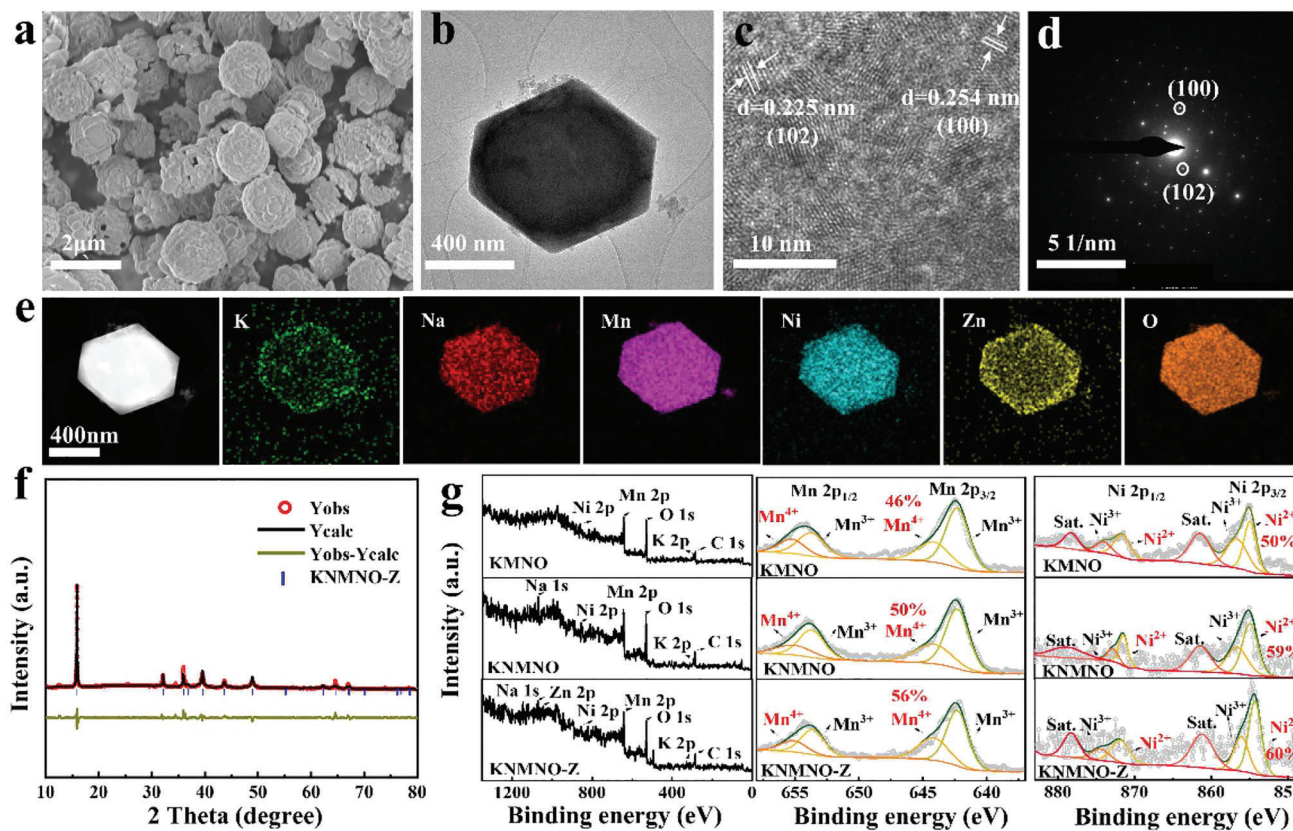


Figure 2. a) SEM image. b) TEM image. c) HR-TEM image. d) SAED pattern. e) Element mapping of KNMNO-Z. f) XRD Rietveld refinement of KNMNO-Z material. g) X-ray photoelectron spectroscopy analysis of three samples: high-resolution spectra of Survey spectrum, Mn 2p and Ni 2p for KMNO, KNMNO, and KNMNO-Z. The binding energies were calibrated against the C1s line of hydrocarbon admixtures (284.8 eV).

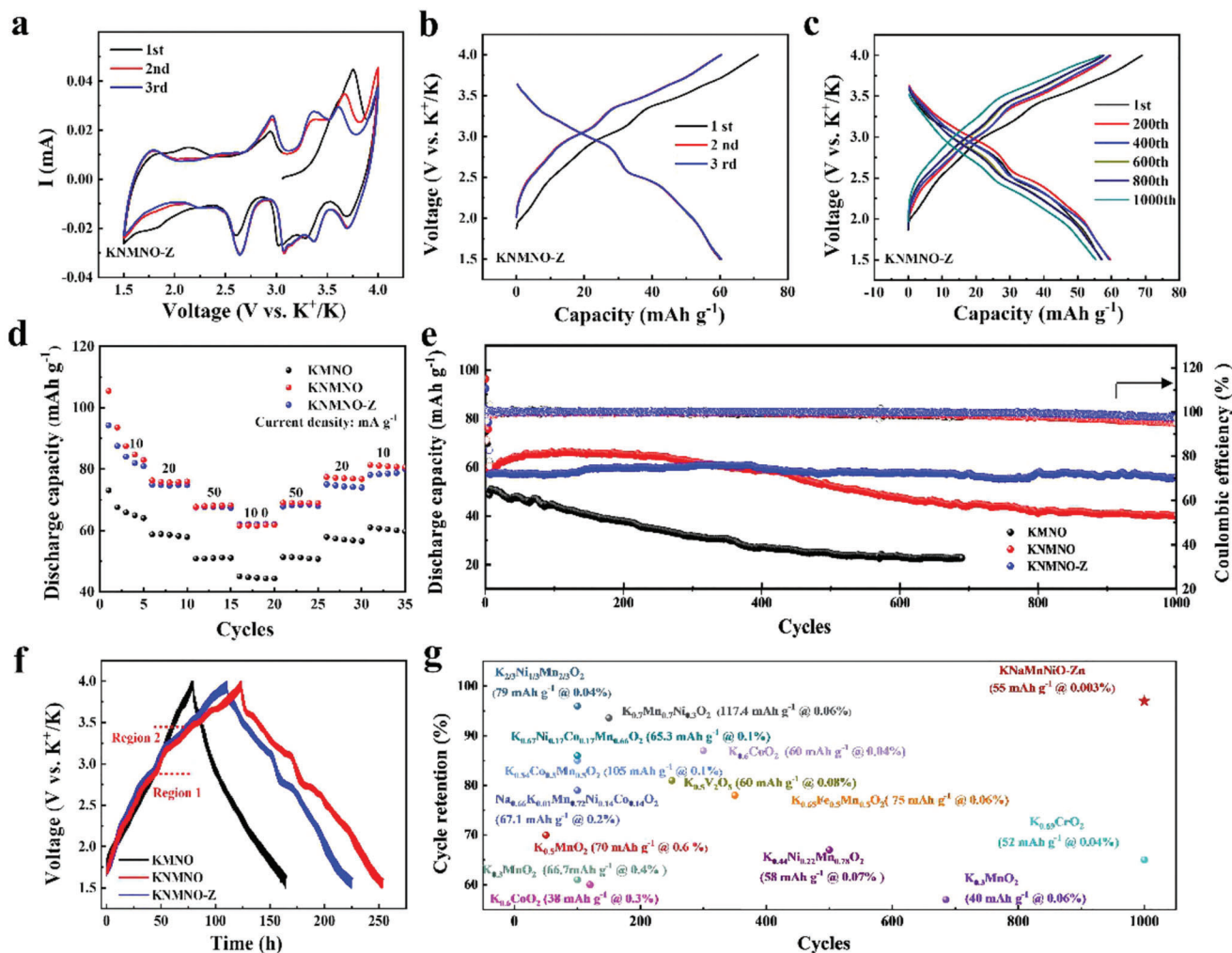


Figure 3. Electrochemical performance of samples in half-cell configuration. a) CV curves for the KNMNO-Z electrode at a scanning rate of 0.1 mV s^{-1} . b,c) Electrochemical charge–discharge curves of KNMNO-Z cathode at a constant current of 100 mA g^{-1} at various cycles. d) Rate capability of KMNO KNMNO, KNMNO-Z. e) Cycling performance of KNMNO-Z at 100 mA g^{-1} . f) GITT profiles for the charge of KMNO, KNMNO, and KNMNO-Z electrode. g) Comparison of the electrochemical performance of KNMNO-Z with previously reported PIBs cathodes.

symmetric P2 material with space group P63/mmc. X-ray photoelectron spectroscopy (XPS) was used to study the oxidation states of transition metals in KMNO, KNMNO, and KNMNO-Z. As shown in Figure 2g, the peaks centered at 642.3 and 653.7 eV correspond to the Mn $2p_{3/2}$ and Mn $2p_{1/2}$ of Mn^{3+} ions, respectively, and the peaks centered at 644.2 and 655.3 eV correspond to the Mn $2p_{3/2}$ and Mn $2p_{1/2}$ of Mn^{4+} ions, respectively.^[31–35] In particular, the partial substitution of Mn by Zn^{2+} and the Mn^{4+} proportion of Mn in KNMNO-Zn (56%) are higher than those of KNMNO (50%), implying a decrease of the Mn valence state upon Zn substitution. The peaks centered at 854.3 and 872.1 eV can be indexed with Ni^{2+} ions, while the peaks at 856.1 and 874.7 eV are indexed with local Ni^{3+} ions. In addition, the satellite peaks of Ni 2p correspond to two wide peaks of 861.2 and 878.7 eV, confirming the presence of local Ni^{3+} ions.^[36,37] After adding Na and Zn ions, the low valence state of Ni becomes prominent (59%–60%), which can facilitate the redox electrochemical reaction and increase its capacity due to two electrons that can be transferred

from bivalent to tetravalent state.^[37,38] The high-resolution spectrum of Zn 2p in KNMNO-Z (Figure S7, Supporting Information) has shown two peaks at 1020.9 and 1043.9 eV, respectively, indicating an effective Zn-doping strategy.^[39,21] The XPS results confirm that Zn doping can reduce the amount of the Jahn–Teller distorted Mn^{3+} centers. In addition, the increase in high-valence Mn is helpful to suppress the dissolution of low-valence Mn and improve its stability. In addition, the higher binding energy of Zn in KNMNO-Z indicates that the Mn–O bond in KNMNO-Z is stronger than that in KNMNO, which may help to improve the phase stability and capacity retention.^[21]

Figure 3a shows the cyclic voltammetry (CV) studies of the electrochemical properties of a series of cathodes at a sweep rate of 0.1 mV s^{-1} between 1.5 and 4.0 V versus K^+/K . KMNO shows no obvious redox peak, indicating a low electrochemical activity without Na. By contrast, KNMNO possesses four pairs of redox peaks, where the two lower voltage peaks (2.6/2.9 V and 3.0/3.4 V) can be assigned to the $\text{Mn}^{3+}/\text{Mn}^{4+}$ redox couple^[40]

and the higher voltage peak between 3.4 and 4.0 V can be attributed to the electrochemical redox reaction of $\text{Ni}^{2+}/\text{Ni}^{3+}$.^[41] This phenomenon suggests that the substitution of Na for K can activate the redox reactions of the transition metals, thereby increasing the electrochemical performance of the material. With the addition of Zn, KNMNO-Z exhibits three pairs of redox peaks probably due to the formation of a stable skeleton structure, thereby inhibiting the structural transformation during K^+ extraction/intercalation. The CV curves of different cycles are consistent with one another, indicating that all samples have a high degree of electrochemical reversibility.^[28,42,43] Figure 3b shows the charge and discharge curves for the initial three cycles at a current density of 100 mA g^{-1} and a voltage range of 1.5–4.0 V, with the first cycle having a discharge capacity of up to 57 mA h g^{-1} . Moreover, the curves of the second and third circles are highly overlapping, which indicates the reversibility of K^+ intercalation and deintercalation. The mechanism of stabilization can be derived from the charge and discharge curves of different cycles (Figure 3c and Figure S8, Supporting Information). After continuous charging and discharging process, the capacity of KMNO gradually decreases and the capacity of KNMNO decreases to some extent. The charging and discharging curves of KNMNO-Z almost overlap, indicating that KNMNO-Z has good reversibility. In Figure 3d, the rate performance of KMNO, KNMNO, and KNMNO-Z was investigated within the range of 1.5–4.0 V. The rate performance also improves with doping strategy, as evidenced by a smaller capacity decrease in KNMNO-Z ($\approx 23\%$) compared with that in KNMNO ($\approx 25\%$) and KNMNO ($\approx 31\%$) when the current density is increased from 10 to 100 mA g^{-1} . At 100 mA g^{-1} , KNMNO-Z showed a higher reversible capacity (62.06 mAh g^{-1}) than KNMNO (61.84 mAh g^{-1}) and KMNO (44.32 mAh g^{-1}). When the current density returned to 10 mA g^{-1} , the average discharge capacity of KNMNO-Z recovered to 79.92 mAh g^{-1} , indicating superior reversibility after the fast K^+ intercalation/deintercalation. In addition, the cycling stability of KMNO, KNMNO, and KNMNO-Z was compared and tested at 100 mA g^{-1} (Figure 3e). The results indicate that Na and Zn-doping contribute to the enhanced capacity and cycling stability. Because the redox-active Mn centers are partially substituted by the redox-inactive Zn dopant in KNMNO-Z, the doped sample exhibits a lower initial capacity than that of KNMNO. Although KNMNO delivered a high discharge capacity in the first 300 cycles, severe capacity fading occurred during discharge due to the Jahn–Teller effect and KMNO had unsatisfactory capacity of K storage. Hence, Na-doping strategy has a crucial role in increasing the redox capacity, and Zn-doping strategy is important in achieving stable cyclability. Remarkably, KNMNO-Z showed a reversible discharge capacity of 57 mAh g^{-1} at 100 mA g^{-1} at the initial cycle, and the capacity remained 97% after 1000 cycles, indicating superior cycling stability upon Na and Zn-doping. Since the redox-active Mn center in KNMNO-Z is partially replaced by the Zn, KNMNO-Z shows lower capacity than KNMNO at the beginning of discharge. However, with repeated charge–discharge cycles, Zn doping in KNMNO achieves excellent capacity retention by inhibiting Jahn–Teller distortion and phase separation, signifying the importance of the Zn dopant in stabilizing the structural stability during the discharge operation. In particular, the KNMNO-Z cathode has an initial Coulombic efficiency (CE) of 82.63%, which is higher than those of KMNO (77.49%)

and KNMNO (75.40%). Meanwhile, the CE after 600 cycles of KMNO (98.30%) and KNMNO (98.96%) were lower than that of KNMNO-Z (99.86%), further demonstrating good electrochemical reversibility. In Figure 3g, compared with other layered oxide cathodes in PIBs, KNMNO-Z shows the smallest capacity attenuation of only 0.003% per cycle,^[1,2,18,28,30,44–52] which represents remarkable electrochemical stability.

The CV curves at scan rates of 0.1, 0.2, 0.3, 0.4, and 0.5 mV s^{-1} were studied to evaluate the storage behavior of K^+ during the electrochemical process. The CV curves have similar shapes and redox peaks at different scan rates, thus affirming efficient and reversible K^+ de/intercalation (Figure S9, Supporting Information). The capacitive behavior of the electrodes was also tested. The peak current (*i*) is correlated with the sweep rate (ν): $I_p = a\nu^b$, where I_p , *a*, *b*, ν are the peak current, regulable parameters (*a*, *b*), and scan rate, respectively. According to previous reports,^[53] the *b* value is close to 1, indicating a pseudo-capacitance process in capacity contribution, while the *b* value is ≈ 0.5 associated with the process of electrochemical diffusion control. In Figure S9b, Supporting Information, all the values of *b* are greater than 0.5, indicating that a considerable portion of pseudo-capacitance participates in the K^+ storage process in the three electrodes.^[54–56] Galvanostatic intermittent titration technique (GITT) was used to analyze the K^+ diffusion coefficient of the electrodes. The GITT data were collected after five cycles of activation in Figure 3f. The GITT-determined discharge–charge curves showed a consistent discharge curve, similar to the galvanostatic discharge (Figure 3b). In Figure 3f, for KNMNO and KNMNO-Z, the charge processes were divided into two regions based on the different electrochemical behavior. In the charging process of 1.5–3.0 V, the D_k^+ (Figure S10, Supporting Information) ranges within 10^{-13} to $10^{-14} \text{ cm}^2 \text{ s}^{-1}$.^[57,58] In the charging process of 3.0–4.0 V, the D_k^+ fast decreases, exhibiting slower reaction kinetics. During the discharge process, it demonstrates a reversible process that the fast K^+ insertion occurs due to the surface process at the beginning and then slowed down with the bulk diffusion. However, KMNO shows a larger diffusion coefficient than KNMNO and KNMNO-Z because the kinetic behavior of KMNO is a pseudo-capacitance behavior, but owning a low capacity and a non-obvious redox reaction, which corresponds to CV (Figure 3a).^[16]

The electrochemical impedance spectra (EIS) of KMNO, KNMNO, and KNMNO-Z were recorded to better understand the dynamic characteristics of the three materials (Figure S11, Supporting Information). The semicircle in the curves represents the R_{ct} , which reflects the migration of K^+ on the surface of active electrode material. Compared with KMNO ($2.0 \times 10^4 \text{ ohm}$) and KNMNO ($1.9 \times 10^4 \text{ ohm}$), KNMNO-Z showed the lowest R_{ct} ($1.2 \times 10^4 \text{ ohm}$), indicating the transfer resistance of K^+ inside KNMNO-Z was the smallest. This finding reveals the faster K^+ transport kinetics during the electrochemical process in KNMNO-Z. Hence, Na and Zn doping in the layered oxide cathode facilitates the movement of potassium ions.^[28,42]

To understand the structural evolution of KNMNO-Z in different charge–discharge states during the first cycle and the second charge, we collected in situ XRD spectra (Figure 4a). At the beginning of the charging, the main peak (002) of the original P2-type structure gradually shifts to a lower angle during the charging process (Figure S12, Supporting Information). This

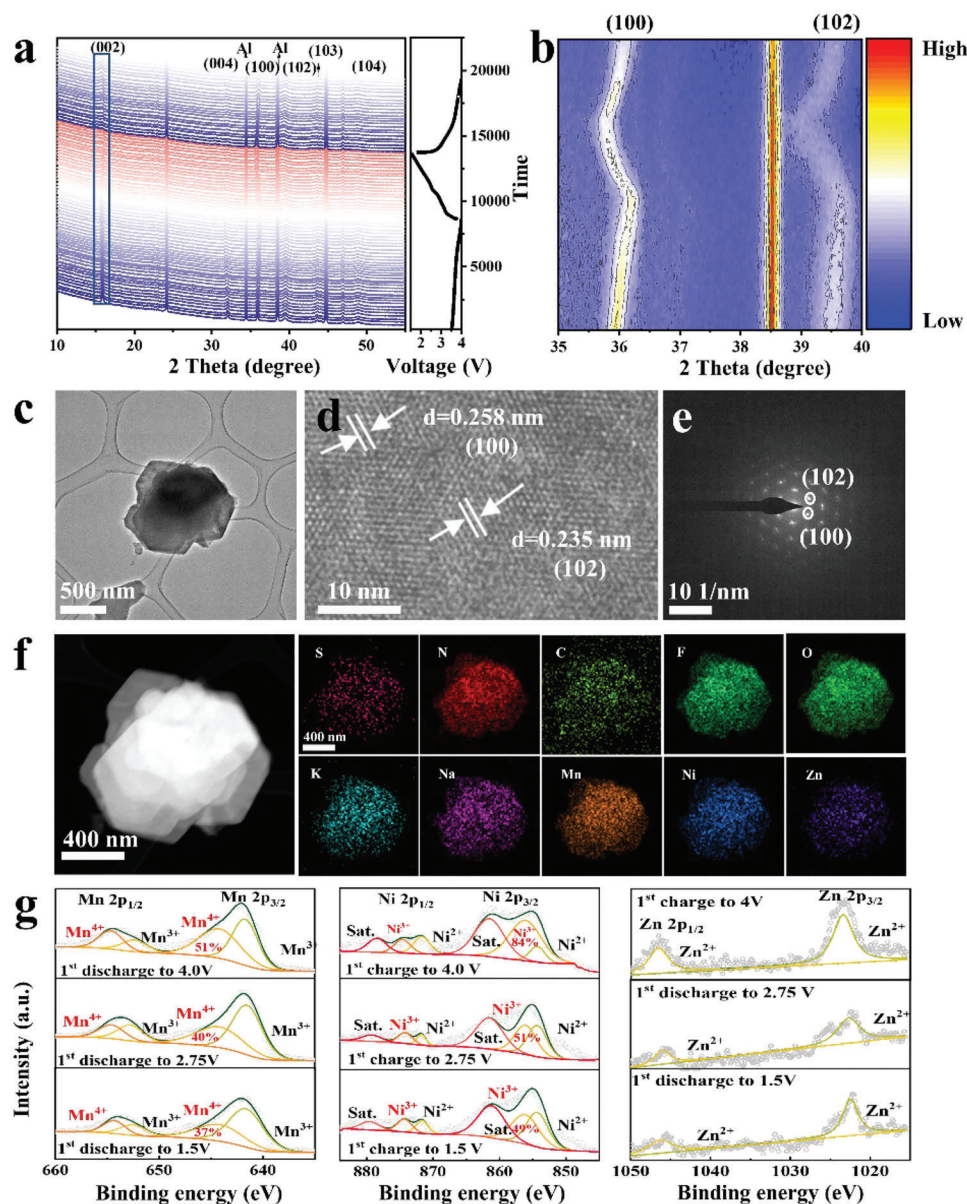


Figure 4. a) In situ XRD patterns combined with electrochemical charge–discharge profile of KNMNO-Z electrode collected during the first and second charge–discharge at 50 mA g⁻¹ in the voltage range of 1.5–4.0 V. b) 2D plot of in situ XRD patterns of KNMNO-Z. c) TEM image. d) HR-TEM image. e) SAED pattern. f) Element mapping of KNMNO-Z harvested from battery after 100 cycles at 100 mA g⁻¹. g) XPS spectra for Ni 2p, Mn 2p, and Zn 2p of P2-KNMNO-Z electrode at different charge states.

phenomenon may be related to the extraction of Na⁺ and K⁺. During the discharge process, the (002) peak returns to its original position, and a new peak appeared at $2\theta = 15$, indicating that the KNMNO-Z electrode has high reversibility and a new potassium-containing P2-type compound, which is beneficial for the improving of electrochemical performance. During the second charging process, the angle of the main peak (002) of the original P2-type structure shifts back to a lower angle, indicating that the composite electrode has high reversibility. In addition, the peaks of (100) and (102) were observed to move toward a higher angle during the second charging process (Figure 4b). The depotassiation may cause the formation of a high-valence transition metal

ion (Mn and Ni element), resulting in a smaller ionic radius relative to its low-valence state. During the discharge process, the structural evolution follows the reverse evolution of potassium removal, which confirms the high reversibility of the structural evolution of KNMNO-Z. However, its mechanism needs to be further studied. In addition, structural properties were investigated by ex situ XRD. The ex situ XRD patterns of KNMNO-Z electrode (Figure S13, Supporting Information) after the first, fifth, and 100th cycles at 100 mA g⁻¹ were determined. The peak of (002), (100), and (102) exhibit no obvious change when compared with pristine material (Figure 2f), indicating its remarkable structural stability during repeated charge–discharge process.^[44,59–62]

Post characterization including TEM and XPS analyses was performed after cycling to further unravel the effect of doping of Zn on the structural stability of KNMNO-Z. In Figure S14, Supporting Information, compared with KMNO, the particle morphologies of KNMNO-Z and KNMNO after 100 cycles of charge and discharge are better preserved. The cross-sectional thickness of the cycled electrode was examined by SEM to investigate the effect of Na and Zn dopants on alleviating the volume expansion after cycling. The calculated volume expansion of the KNMNO-Z electrode dropped monotonically to 25% compared with those of KMNO (39%) and KNMNO (30%) (Figure S15, Supporting Information). The results confirm the positive effect of the introduction of Na and Zn dopant in alleviating volume changes. TEM was used to study the composition and chemical element distribution in particles after the repeated electrochemical reaction. In Figure 4c, the phase structures of KNMNO-Z after 100 cycles at 100 mA g⁻¹ can be well maintained, indicating the impressive stability of KNMNO-Z. In Figure 4d, the HRTEM analysis suggests clear lattice fringes with interplanar spacings of 0.225 and 0.255 nm, which can be ascribed to the (102) and (100) planes of the typical P2-type layered structure, consistent with original materials (Figure 2d) and demonstrates the stability of the KNMNO-Z structure. As shown in Figure 4f, Figures S16 and S17, and Table S2, Supporting Information, a small amount of Na ions were observed after the first charging and discharging process, indicating that Na⁺ are not completely replaced by K⁺ after the first charging and discharging. Residual Na ions are found in the ion exchanged layered oxide even after 100 cycles of charging–discharging process. These results indicate that the residual Na ions in the K-layered oxide can contribute to enhanced electrochemical performance.^[63] In Figures 4g and S18, we also studied the transition metal valence in KNMNO-Z and KNMNO during the charge–discharge process by ex situ XPS measurement. For KNMNO-Zn, when charged to 4.0 V, the ratio of Ni³⁺ increases, indicating that Ni²⁺ is oxidized. When discharged to 2.75 and 1.5 V, the ratio of Ni³⁺ decreases, indicating the reduction process of Ni²⁺. For Mn, the Mn⁴⁺ peak intensity increases with the decrease of Mn³⁺ peak intensity when charging to 4.0 V, indicating the oxidation of Mn³⁺ into Mn⁴⁺ in Figure 4g. The Mn³⁺ contains 49% of the total amount at the charge state of 4.0 V. During the following discharge, the intensity of Mn³⁺ peak gradually increases, which proves the reduction of Mn⁴⁺ to Mn³⁺.^[28,64,65]

The interfacial performance of KNMNO-Z electrodes at different charging stages was studied by Electrochemical impedance spectroscopy (EIS) method (Figure 5a). After 1 to 5 cycles, the R_{ct} increases, which belongs to the process of electrode activation, after 100 cycles, and the electrode has a slight deterioration (inset of Figure 5a). From the TEM tests, the working electrode shows a uniform cathode electrolyte interphase (CEI) layer of 7–8 nm after 100 cycles, in stark contrast to the bare surface of the original KNMNO-Z electrode (Figure 5b,c).^[66,67] XPS analysis was conducted to reveal the chemical compositions of the CEI films formed on the surfaces of the KNMNO-Z electrodes in 2.5 M KFSI/TEP electrolytes after 100 cycles (Figure 5d). The CEI shows the presence of C, K, F, S, N, and O corresponding the compounds such as KF, potassium sulfur oxynitride (KSON), K₂SO₄, K₂SO₃ and S due to the decomposition of KFSI salt.^[68–70] The formation of KF rich CEI compound may enhance the structural stability of the KNMNO-Z and lead to high cycling stability

Density functional theory (DFT) calculations were conducted to investigate electronic structure, and charge density in P2-KNMNO-Z. The optimized structures of KNMNO and KNMNO-Z based on the Rietveld refinement of XRD data are displayed in Figure 5e. The geometry optimization of KNMNO was performed within a supercell, which consists of 2 K, 23 Mn, 62 Na, 9 Ni, and 64 O atoms. For KNMNO-Z, the position of the Mn atom in the optimized KNMNO is replaced by the Zn atom, and the position of the Na atom is replaced by part of the K atom. In KNMNO, the longest bond length of Mn–O is 2.18800 Å, and the shortest bond length is 1.85573 Å, the distortion of Mn–O is 0.33227 Å, while in KNMNO, the longest bond length of Mn–O and the shortest bond length are 1.96191 Å and 1.92525 Å, the distortion of Mn–O is 0.03666 Å. The distortion of KNMNO-Z was smaller than that of KNMNO because the anisotropy difference of bond length is small. In addition, the partial charge density distribution in Figure 5f reflects the local status of electrons. The charge density of Mn–O reflects that the interaction between Mn and O is more intense after Zn doping. The density of states (DOS) of the KNMNO and KNMNO-Z are plotted in Figure 5g to illustrate the electronic behavior. From the total DOS, the Zn dopant contributes largely to the total DOS of the system, including the states ≈–0.8, –0.2, and 1.0–3.0 eV. Zn orbitals are overlapped with the O 2p orbital close to the Fermi level that deform the electronic property of the KNMNO-Z system largely, suggesting that Zn substitution can modulate the electronic structure around Mn–O bonding and thus alleviate the anisotropic coupling between oxidized O²⁻ and Mn⁴⁺.^[71] In addition, the atomic DOS shows strong orbital hybridizations between the Mn 2p orbital and the Zn 2p orbital at ≈–4.5 eV while between the Mn 2p orbital and the O 1s orbital at ≈–6.0 eV and the Fermi level, which illustrates the strong binding force of Mn–Zn and Mn–O bonds. This result is in good agreement with the findings based on the geometric structure and charge density distribution (Figure 5f). As a result, the introduction of Zn would alleviate the lattice distortion, resulting in good structural stability and K storage performance.

The full cell was assembled using KNMNO-Z and hard carbon as the cathode and anode, respectively (Figure 6a). Hard carbon was commercially purchased, and its XRD pattern and electrochemical performance in the half-cell PIBs were analyzed before it was used in the full cell (Figure S19, Supporting Information). The galvanostatic discharge–charge curves of the hard carbon in Figure S19b, Supporting Information, which showed an average discharge platform of ≈0.5 V. The non-inflammable TEP electrolyte was selected as the electrolyte, and the voltage range of charging and discharging was from 1.0 to 3.5 V. The hard carbon without any pre-treatment showed good cycling stability in the half-cell PIBs in the TEP-based electrolyte and delivered the reversible specific capacity of 100.7 mA h g⁻¹ at 100 mA g⁻¹ after 300 cycles (Figure S19c, Supporting Information). The activated KNMNO-Z electrodes were used to assemble full cells with fresh hard carbon electrodes. In Figure 6b, the CV curves of the full cells were conducted. The CV curves of the full cell showed multiple cathodic and anodic peaks within the voltage range of 1.0–3.5 V at the scan rate of 0.1 mV s⁻¹, which reflected the different potassiation depths of KNMNO-Z. The galvanostatic discharge–charge curves of the full cell showed an average discharge platform of ≈1.5 V showing the good performance

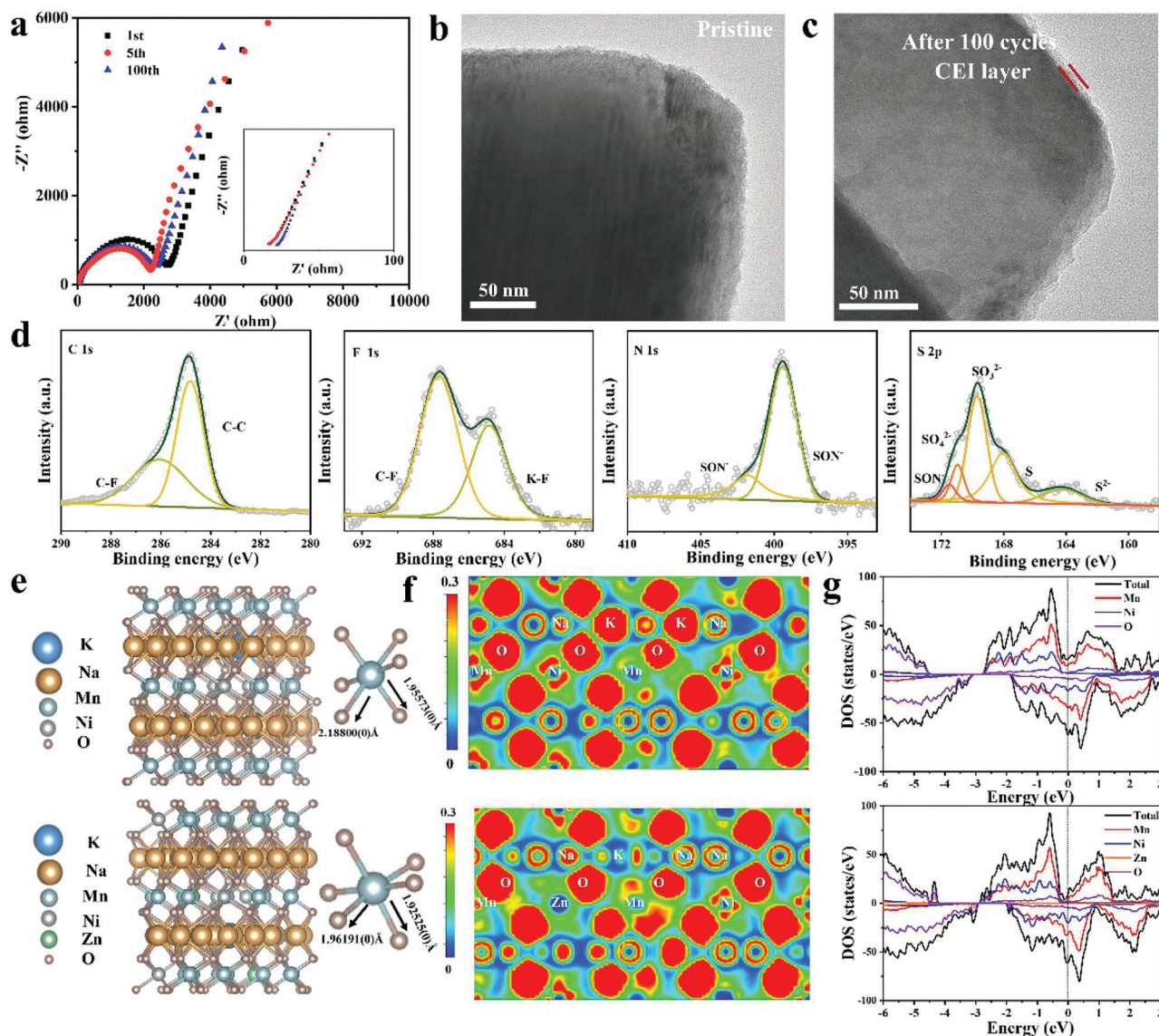


Figure 5. a) EIS at charged state after different cycles with the inset of partial enlarged figure. b) HRTEM images of pristine KNMNO-Z cathode and KNMNO-Z. c) harvested from battery after 100 cycles. d) C 1s, F 1s, N 1s, and S 2p XPS spectra of cycled KNMNO-Z. e) Optimized structure of KNMNO and KNMNO-Z, respectively; the enlarged insets show the octahedral MO_6 units, as well as equatorial and axial bonds. f) Charge density distribution for KNMNO and KNMNO-Z (visualized by Visualization for Electronic and Structure Analysis (VESTA)), the red regions stand for high charge density and blue regions for low charge density. g) Total density of states (tDOS) and partial density of states (pDOS) of Mn, Ni, O, or/and Zn orbitals for KNMNO and KNMNO-Z.

(Figure 6c). Figure 6d shows the rate performance of the full cell. The average capacities were 76.46, 69.47, 61.8, and 55.79 mAh g^{-1} at the current densities of 10, 20, 50, and 100 mA g^{-1} , respectively. The K-based full cell delivers an initial charge and discharge capacities of 52.05 and 52.58 mAh g^{-1} owing to the formation of solid-state interfacial film by irreversible interfacial storage. Encouragingly, CE is greatly improved to 99.94% after the activation of some cell components in 200 cycles. The retained capacity was 43.68 mA h g^{-1} after 50 cycles at 100 mA g^{-1} (Figure 6e). A fan can be turned by a coin-type full cell, indicating potential in practical applications (Figure 6e).

3. Conclusion

KNMNO-Z with a P2-type structure was synthesized by solid phase method. According to the experimental results, Zn doping has two positive effects on KNMNO. First, Zn^{2+} would primarily result in Jahn–Teller distortion of Mn^{3+} . Second, the doping of Zn^{2+} makes the phase stability of the P2 structure robust during the charging and discharging process, thus preventing its phase transition. Based on DFT, Zn substitution can regulate the electronic structure around the Mn–O bond, thereby alleviating the anisotropic coupling between oxidized O^{2-} and Mn^{4+} .

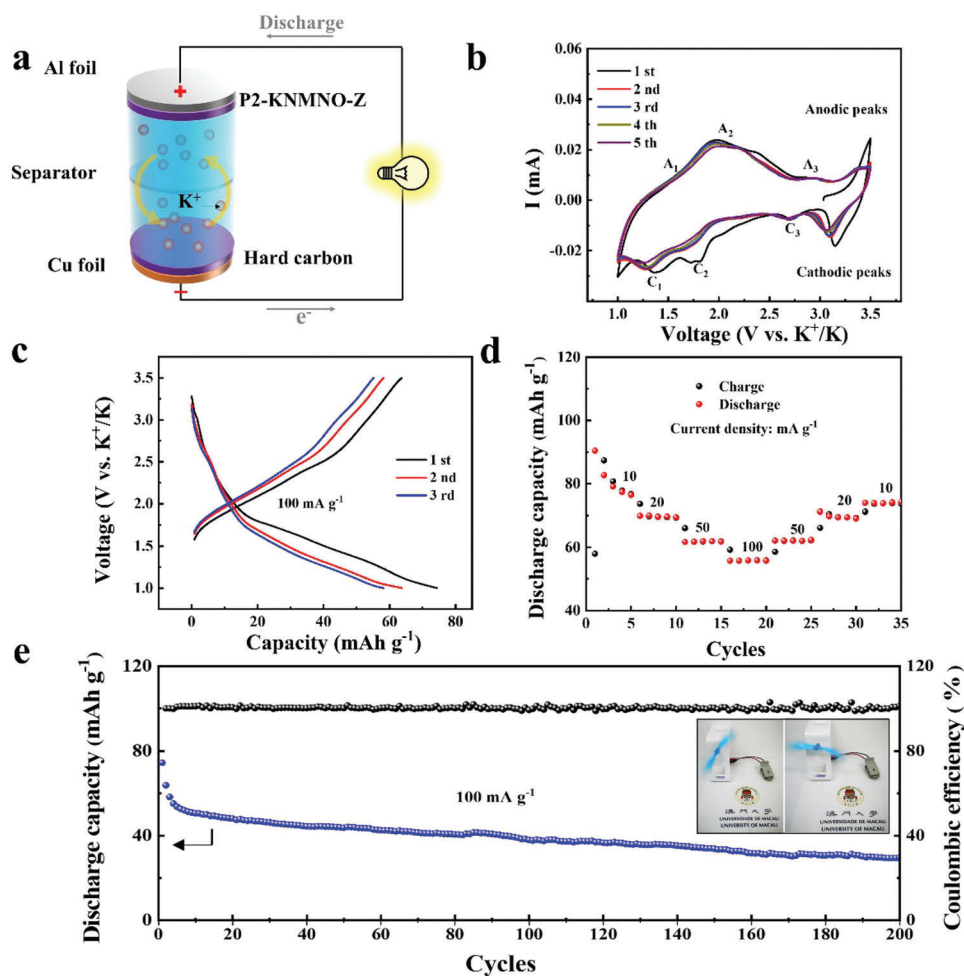


Figure 6. Demonstration of PIBs based on P2-KNMNO-Z/hard carbon configuration: a) schematic illustration of the PIBs. b) First five cycles of CV measurements of the full cell. c) Galvanostatic discharge–charge curves of the full cell, cycled at a current rate of 100 mA g^{-1} . d) Cycle performance of the full cell at the current density of 100 mA g^{-1} . e) Optical photos of the full cell powering an electric fan. All the current densities and capacities were normalized by the weight of active material on the cathode side. The full cell tests were performed in the voltage range of 1.0–3.5 V at room temperature.

Therefore, KNMNO-Z has obvious phase stability and capacity retention ability compared with KNMNO. Finally, KNMNO-Z has good cycle stability with high capacity retention of 97% after 1000 cycles at 100 mA g^{-1} , and the decay rate of each cycle is only 0.003%. Therefore, zinc doping may be an effective and widely used strategy for manganese-based cathode materials for PIBs.

4. Experimental Section

Preparation of $\text{Mn}_{0.75}\text{Ni}_{0.25}\text{CO}_3$: Manganese acetate ($\text{Mn}(\text{CH}_3\text{COO})_2 \cdot 4\text{H}_2\text{O}$, AR) and nickel acetate ($\text{Ni}(\text{CH}_3\text{COO})_2 \cdot 4\text{H}_2\text{O}$, AR) were dissolved with 1.45 g of urea in a stoichiometric ratio of 39 mL H_2O and 26 mL ethanol to form a mixed solution. The solution was then transferred into a 100 mL Teflon-lined autoclave and stored at 180°C for 24 h. After filtration, wash several times with H_2O and alcohol, and dry at 60°C to obtain $\text{Mn}_{0.75}\text{Ni}_{0.25}\text{CO}_3$ precursor.

Synthesis of KNMNO-Z: $\text{Mn}_{0.75}\text{Ni}_{0.25}\text{CO}_3$ precursor was homogeneously mixed with K_2CO_3 , ZnO, NaCl, and KCl. Then, the mixture was calcined in air at 800°C for 12 h and quenched to room temperature. Finally, the product was obtained by washing, filtering, and drying. The sample was named KNMNO-Z.

Material Characterization: Use the X-ray diffractometer (Rigaku Smartlab 9000 W) with a Cu-target ($\lambda = 1.54181 \text{ \AA}$) at the scan rate of $10^\circ \text{ min}^{-1}$ to obtain all XRD data. Use field emission scanning electron microscope (FESEM, JEOL JSM-7500FA) to observe the morphologies of all samples. XPS analysis of monochromatic Al $K\alpha$ radiation (excitation energy of 1486 eV) was performed on the Thermo ESCALAB 250 spectrometry platform.

Electrochemical Measurements: The active substance, acetylene black, and PVDF were mixed in an 8:1:1 mass ratio to obtain an electrode in NMP. The above mixture is stirred magnetically to form a homogeneous slurry. The mixture was then coated on Al foil. Place these wet electrodes in an oven, initially dry at 60°C for 2 h, then transfer to a vacuum oven for 8 h at 90°C . All dry electrodes were pressed into a disk $\Phi 12 \text{ mm}$ for further testing. The coin-type half-battery (CR2032) was assembled in an Ar-filled glove box (Lab2000, Etelux) and its electrochemical properties are analyzed. Assemble the half-cell with potassium metal and glass microfibers (GF/D, Whatman) as counter electrodes and separators, respectively, and 2.5 m KFSI dissolved in triethyl phosphate (TEP) solution as the electrolyte. Battery performance was characterized using the Neware CT-4000 Battery Test System (Shenzhen, China). Cyclic voltammetry (CV) was performed at room temperature using an electrochemical workstation (VMP-300 biological system, Germany) at a scanning rate of $0.1\text{--}0.5 \text{ mV s}^{-1}$ between 1.5 and 4.0 V (vs K^+/K)

The GITT was performed at a pulsed current of 100 mA g⁻¹ for 30 min and then rested for 1 h. This process was repeated several times until a pre-set potential was reached. All cells were cyclically activated at 10 mA g⁻¹ for 5 cycles prior to testing. The ion diffusion coefficient (D_{k^+}) was calculated by the following equation:

$$D = \frac{4}{\pi\tau} \left(\frac{m_s V_M}{M_s S} \right)^2 \left(\frac{\Delta E_s}{\tau \times \frac{dE_s}{d\sqrt{\tau}}} \right)^2 \left(\tau \ll \frac{L^2}{D} \right) \quad (1)$$

where τ , m_s , V_M , M_s , S , are the period of the pulse, the active mass of the electrode, the molar volume of the active material, the molar mass of the electrode material, and the area of the electrode, respectively. M_s/V_M is calculated from the electrode density, and L is the average thickness of the electrode. ($\tau = 1800$ s, $S = 1.13$ cm²)

To assemble full-cell, a KNMNO-Z was selected as the cathode and hard carbon as the anode. Hard carbon was commercially purchased. The active material, acetylene black, and PVDF with a weight ratio of 7:2:1 were mixed in NMP (N-methyl-2-pyrrolidone) to prepare the anode electrode. 2.5 m KFSI-TEP electrolyte was used as the electrolyte. The capacity was calculated based on cathode materials. The hard carbon anode was prepotassiated for 5 cycles at a current of 50 mA g⁻¹ to assemble the full-cell. The full-cell was analyzed in a voltage window of 1.0–3.5 V. (Note: N/P ratio is 1.2).

Computational Methods: DFT calculations were performed using the Vienna abinitio simulation package (VASP). The calculations use the PBE exchange-correlation functional, which was a generalized gradient approximation (GGA) method. Since GGA cannot correctly reproduce the localized electronic states of transition metal oxide materials, the GGA + U method was used. The U values of Mn and Ni were 3.9 and 6.9 eV, respectively. Plane-wave projector augmented wave (PAW) pseudo-potentials were used to represent the core electrons. In all calculations, the plane wave energy cutoff was 400 eV.

Supporting Information

Supporting Information is available from the Wiley Online Library or from the author.

Acknowledgements

Y.Z. and J.L. contributed equally to this work. This work was funded by The Science and Technology Development Fund, Macau SAR (File no. 046/2019/AFJ, 0007/2021/AGJ, 006/2022/ALC), the Multi-Year Research Grants (MYRG2020-00187-IAPME and MYRG2022-00223-IAPME) from the Research Services and Knowledge Transfer Office at the University of Macau, and the UEA funding, the Science and Technology Program of Guangdong Province of China (Grant No. 2022A0505030028), the Science and Technology Innovation Committee of Shenzhen Municipality (SGDX20201103093600003). The DFT calculations are performed at High Performance Computing Cluster (HPCC) of Information and Communication Technology Office (ICTO) at University of Macau.

Conflict of Interest

The authors declare no conflict of interest.

Data Availability Statement

The data that support the findings of this study are available from the corresponding author upon reasonable request.

Keywords

Jahn–Teller distortion, K_{0.02}Na_{0.55}Mn_{0.70}Ni_{0.25}Zn_{0.05}O₂ cathodes, Mn-based layered oxide, Zn-doping strategy

Received: March 20, 2023

Revised: April 3, 2023

Published online: May 10, 2023

- [1] Z. Xiao, J. Meng, F. Xia, J. Wu, F. Liu, X. Zhang, L. Xu, X. Lin, L. Mai, *Energy Environ. Sci.* **2020**, *13*, 3129.
- [2] X. Zhang, Y. Yang, X. Qu, Z. Wei, G. Sun, K. Zheng, H. Yu, F. Du, *Adv. Funct. Mater.* **2019**, *29*, 1905679.
- [3] X. Min, J. Xiao, M. Fang, W. Wang, Y. Zhao, Y. Liu, A. M. Abdelkader, K. Xi, R. V. Kumar, Z. Huang, *Energy Environ. Sci.* **2021**, *14*, 2186.
- [4] J.-Y. Hwang, S.-T. Myung, Y.-K. Sun, *Adv. Funct. Mater.* **2018**, *28*, 1802938.
- [5] P.-F. Wang, H.-R. Yao, X.-Y. Liu, Y.-X. Yin, J.-N. Zhang, Y. Wen, X. Yu, L. Gu, Y.-G. Guo, *Sci. Adv.* **2018**, *4*, eaar6018.
- [6] T. Hosaka, K. Kubota, A. S. Hameed, S. Komaba, *Chem. Rev.* **2020**, *120*, 6358.
- [7] Z. Zhang, Q. Hu, J. Liao, Y. Xu, L. Duan, R. Tian, Y. Du, J. Shen, X. Zhou, *Nano Lett.* **2023**, *23*, 694.
- [8] H. Wang, H. Peng, Z. Xiao, R. Yu, F. Liu, Z. Zhu, L. Zhou, J. Wu, *Energy Storage Mater.* **2023**, *58*, 101.
- [9] Z. Liu, H. Su, Y. Yang, T. Wu, S. Sun, H. Yu, *Energy Storage Mater.* **2021**, *34*, 211.
- [10] H. Kim, J. C. Kim, M. Bianchini, D. H. Seo, J. Rodriguez-Garcia, G. Ceder, *Adv. Energy Mater.* **2017**, *8*, 1702384.
- [11] W. Li, Z. Bi, W. Zhang, J. Wang, R. Rajagopalan, Q. Wang, D. Zhang, Z. Li, H. Wang, B. Wang, *J. Mater. Chem. A* **2021**, *9*, 8221.
- [12] L. Wu, H. Fu, S. Li, J. Zhu, J. Zhou, A. M. Rao, L. Cha, K. Guo, S. Wen, B. Lu, *Nat. Commun.* **2023**, *14*, 644.
- [13] L. Deng, T. Wang, Y. Hong, M. Feng, R. Wang, J. Zhang, Q. Zhang, J. Wang, L. Zeng, Y. Zhu, L. Guo, *ACS Energy Lett.* **2020**, *5*, 1916.
- [14] Q. C. Wang, J. K. Meng, X. Y. Yue, Q. Q. Qiu, Y. Song, X. J. Wu, Z. W. Fu, Y. Y. Xia, Z. Shadike, J. Wu, X. Q. Yang, Y. N. Zhou, *J. Am. Chem. Soc.* **2019**, *141*, 840.
- [15] C. Heubner, B. Matthey, T. Lein, F. Wolke, T. Liebmann, C. Lämmel, M. Schneider, M. Herrmann, A. Michaelis, *Energy Storage Mater.* **2020**, *27*, 377.
- [16] F. Fu, X. Liu, X. Fu, H. Chen, L. Huang, J. Fan, J. Le, Q. Wang, W. Yang, Y. Ren, K. Amine, S. G. Sun, G. L. Xu, *Nat. Commun.* **2022**, *13*, 2826.
- [17] Q. Shi, R. Qi, X. Feng, J. Wang, Y. Li, Z. Yao, X. Wang, Q. Li, X. Lu, J. Zhang, Y. Zhao, *Nat. Commun.* **2022**, *13*, 3205.
- [18] M. G. T. Nathan, N. Naveen, W. B. Park, K.-S. Sohn, M. Pyo, *J. Power Sources* **2019**, *438*, 226992.
- [19] K. Wang, Z.-G. Wu, T. Zhang, Y.-P. Deng, J.-T. Li, X.-D. Guo, B.-B. Xu, B.-H. Zhong, *Electrochim. Acta* **2016**, *216*, 51.
- [20] Z. Xiao, F. Xia, L. Xu, X. Wang, J. Meng, H. Wang, X. Zhang, L. Geng, J. Wu, L. Mai, *Adv. Funct. Mater.* **2021**, *32*, 2108244.
- [21] K. Zhang, D. Kim, Z. Hu, M. Park, G. Noh, Y. Yang, J. Zhang, V. W. Lau, S. L. Chou, M. Cho, S. Y. Choi, Y. M. Kang, *Nat. Commun.* **2019**, *10*, 5203.
- [22] Y. Liu, C. Wang, S. Zhao, L. Zhang, K. Zhang, F. Li, J. Chen, *Chem. Sci.* **2020**, *12*, 1062.
- [23] P. Wang, T. Jin, J. Zhang, Q. Wang, X. Ji, C. Cui, N. Piao, S. Liu, J. Xu, X. Yang, C. Wang, *Nano Energy* **2020**, *77*, 105167.
- [24] Y.-S. Xu, Q.-H. Zhang, D. Wang, J.-C. Gao, X.-S. Tao, Y. Liu, Y.-G. Sun, L. Gu, B.-B. Chang, C.-T. Liu, S.-Q. Shi, A.-M. Cao, *Energy Storage Mater.* **2020**, *31*, 20.
- [25] M. K. Cho, J. H. Jo, J. U. Choi, S. T. Myung, *ACS Appl. Mater. Interfaces* **2019**, *11*, 27770.

- [26] P. Bai, K. Jiang, X. Zhang, J. Xu, S. Guo, H. Zhou, *ACS Appl. Mater. Interfaces* **2020**, *12*, 10490.
- [27] Q. Zhang, C. Didier, W. K. Pang, Y. Liu, Z. Wang, S. Li, V. K. Peterson, J. Mao, Z. Guo, *Adv. Energy Mater.* **2019**, *9*, 1900568.
- [28] C.-I. Liu, S.-h. Luo, H.-b. Huang, Y.-c. Zhai, Z.-w. Wang, *Electrochim. Acta* **2018**, *286*, 114.
- [29] D. Luo, X. Ding, X. Hao, H. Xie, J. Cui, P. Liu, X. Yang, Z. Zhang, J. Guo, S. Sun, Z. Lin, *ACS Energy Lett.* **2021**, *6*, 2755.
- [30] T. Deng, X. Fan, C. Luo, J. Chen, L. Chen, S. Hou, N. Eidson, X. Zhou, C. Wang, *Nano Lett.* **2018**, *18*, 1522.
- [31] J. Xie, L. Gao, S. Cao, W. Liu, F. Lei, P. Hao, X. Xia, B. Tang, *J. Mater. Chem. A* **2019**, *7*, 13577.
- [32] Z. Xiao, J. Meng, Q. Li, X. Wang, M. Huang, Z. Liu, C. Han, L. Mai, *Sci. Bull.* **2018**, *63*, 46.
- [33] S. Bao, S. Luo, Z. Wang, Q. Wang, A. Hao, Y. Zhang, Y. Wang, *J. Power Sources* **2017**, *362*, 323.
- [34] Q. Li, G. Li, C. Fu, D. Luo, J. Fan, L. Li, *ACS Appl. Mater. Interfaces* **2014**, *6*, 10330.
- [35] J.-W. Shi, C. Gao, C. Liu, Z. Fan, G. Gao, C. Niu, *J Nanopart Res* **2017**, *19*, 194.
- [36] S. Chen, Z. Liao, J. Kang, Y. Zhang, S. Zhi, X. Cai, W. Yang, H. Zou, W. Yang, *J. Alloys Compd.* **2022**, *910*, 164793.
- [37] H. Zhu, T. Xie, Z. Chen, L. Li, M. Xu, W. Wang, Y. Lai, J. Li, *Electrochim. Acta* **2014**, *135*, 77.
- [38] H. Wang, W. Ge, W. Li, F. Wang, W. Liu, M. Z. Qu, G. Peng, *ACS Appl. Mater. Interfaces* **2016**, *8*, 18439.
- [39] B. Peng, Y. Chen, F. Wang, Z. Sun, L. Zhao, X. Zhang, W. Wang, G. Zhang, *Adv. Mater.* **2022**, *34*, 2103210.
- [40] I. Hasa, D. Buchholz, S. Passerini, B. Scrosati, J. Hassoun, *Adv. Energy Mater.* **2014**, *4*, 1400083.
- [41] S. Doubajji, M. Valvo, I. Saadoun, M. Dahbi, K. Edström, *J. Power Sources* **2014**, *266*, 275.
- [42] C. Liu, S. Luo, H. Huang, Z. Wang, A. Hao, Y. Zhai, Z. Wang, *Electrochim. Commun.* **2017**, *82*, 150.
- [43] B. Qiu, J. Wang, Y. Xia, Y. Liu, L. Qin, X. Yao, Z. Liu, *J. Power Sources* **2013**, *240*, 530.
- [44] H. Kim, D. H. Seo, J. C. Kim, S. H. Bo, L. Liu, T. Shi, G. Ceder, *Adv. Mater.* **2017**, *29*, 1702480.
- [45] T. Deng, X. Fan, J. Chen, L. Chen, C. Luo, X. Zhou, J. Yang, S. Zheng, C. Wang, *Adv. Funct. Mater.* **2018**, *28*, 1800219.
- [46] C. Vaalma, G. A. Giffin, D. Buchholz, S. Passerini, *J. Electrochem. Soc.* **2016**, *163*, A1295.
- [47] J. U. Choi, J. Kim, J.-Y. Hwang, J. H. Jo, Y.-K. Sun, S.-T. Myung, *Nano Energy* **2019**, *61*, 284.
- [48] K. Wang, Z.-G. Wu, T. Zhang, Y.-P. Deng, J.-T. Li, X.-D. Guo, B.-B. Xu, B.-H. Zhong, *Electrochim. Acta* **2016**, *216*, 51.
- [49] C.-L. Liu, S.-H. Luo, H.-B. Huang, Y.-C. Zhai, Z.-W. Wang, *Chem. Eng. J.* **2019**, *356*, 53.
- [50] H. Kim, J. C. Kim, S. H. Bo, T. Shi, D. H. Kwon, G. Ceder, *Adv. Energy Mater.* **2017**, *7*, 1700098.
- [51] J.-Y. Hwang, J. Kim, T.-Y. Yu, S.-T. Myung, Y.-K. Sun, *Energy Environ. Sci.* **2018**, *11*, 2821.
- [52] L. Deng, X. Niu, G. Ma, Z. Yang, L. Zeng, Y. Zhu, L. Guo, *Adv. Funct. Mater.* **2018**, *28*, 1800670.
- [53] Z. Zhang, B. Xi, X. Wang, X. Ma, W. Chen, J. Feng, S. Xiong, *Adv. Funct. Mater.* **2021**, *31*, 2103070.
- [54] Y. Jiang, Y. Wang, X. Li, J. Zhang, K. Chen, J. Liang, L. Zhao, C. Dai, *Colloids Surf. A* **2022**, *649*, 129340.
- [55] L. Sun, Y. Xie, X. Z. Liao, H. Wang, G. Tan, Z. Chen, Y. Ren, J. Gim, W. Tang, Y. S. He, K. Amine, Z. F. Ma, *Small* **2018**, *14*, 1704523.
- [56] H. Yang, R. Xu, Y. Yao, S. Ye, X. Zhou, Y. Yu, *Adv. Funct. Mater.* **2019**, *29*, 1809195.
- [57] J. H. Jo, J. Y. Hwang, J. Choi, Y. K. Sun, S. T. Myung, *ACS Appl. Mater. Interfaces* **2019**, *11*, 43312.
- [58] S. Zhao, K. Yan, J. Liang, Q. Yuan, J. Zhang, B. Sun, P. Munroe, G. Wang, *Adv. Funct. Mater.* **2021**, *31*, 2102060.
- [59] X. Huang, D. Li, H. Huang, X. Jiang, Z. Yang, W. Zhang, *Nano Res.* **2021**, *14*, 3531.
- [60] B. Peng, Z. Sun, L. Zhao, J. Li, G. Zhang, *Energy Storage Mater.* **2021**, *35*, 620.
- [61] B. Xiao, K. Wang, G. L. Xu, J. Song, Z. Chen, K. Amine, D. Reed, M. Sui, V. Sprenkle, Y. Ren, P. Yan, X. Li, *Adv. Mater.* **2019**, *31*, 1805889.
- [62] Y. Liu, Q. Shen, X. Zhao, J. Zhang, X. Liu, T. Wang, N. Zhang, L. Jiao, J. Chen, L. Z. Fan, *Adv. Funct. Mater.* **2019**, *30*, 1907837.
- [63] H. Kim, Y.-W. Byeon, J. Wang, Y. Zhang, M. C. Scott, K. Jun, Z. Cai, Y. Sun, *Energy Storage Mater.* **2022**, *47*, 105.
- [64] S. Zhao, K. Yan, P. Munroe, B. Sun, G. Wang, *Adv. Energy Mater.* **2019**, *9*, 1803757.
- [65] C. Wang, L. Liu, S. Zhao, Y. Liu, Y. Yang, H. Yu, S. Lee, G. H. Lee, Y. M. Kang, R. Liu, F. Li, J. Chen, *Nat. Commun.* **2021**, *12*, 2256.
- [66] C. Yang, X. Zhang, J. Huang, P. Ao, G. Zhang, *Electrochim. Acta* **2016**, *196*, 261.
- [67] S. N. Lim, J. Y. Seo, D. S. Jung, W. Ahn, H. S. Song, S.-H. Yeon, S. B. Park, *J. Alloys Compd.* **2015**, *623*, 55.
- [68] Q. Zhang, J. Mao, W. K. Pang, T. Zheng, V. Sencadas, Y. Chen, Y. Liu, Z. Guo, *Adv. Energy Mater.* **2018**, *8*, 1703288.
- [69] S. Liu, J. Mao, Q. Zhang, Z. Wang, W. K. Pang, L. Zhang, A. Du, V. Sencadas, W. Zhang, Z. Guo, *Angew. Chem., Int. Ed. Engl.* **2020**, *59*, 3638.
- [70] H. Wang, D. Zhai, F. Kang, *Energy Environ. Sci.* **2020**, *13*, 4583.
- [71] Y. Ling, J. Zhou, S. Guo, H. Fu, Y. Zhou, G. Fang, L. Wang, B. Lu, X. Cao, S. Liang, *ACS Appl. Mater. Interfaces* **2021**, *13*, 58665.